applied sciences

MDPI

Article

Luminescent Properties of Silicon Nanocrystals:Spin on Glass Hybrid Materials

Marco Antonio Vásquez-Agustín [1], Orlando Cortazar-Martínez [1], Alfredo Abelardo González-Fernández [1], José Alberto Andraca-Adame [2], Alfredo Morales-Sánchez [3,*] and Mariano Aceves-Mijares [1,*]

1 Departamento de Electronica, Instituto Nacional de Astrofísica, Óptica y Electrónica (INAOE), Tonantzintla, 72840 Cholula, Puebla, Mexico; mava.vasquez@gmail.com (M.A.V.-A.); or.ing07@gmail.com (O.C.-M.); chachogf@gmail.com (A.A.G.-F.)

2 Instituto Politécnico Nacional, CNMN, Avenida Luis Enrique Erro S/N, Zacatenco, Delegación Gustavo Adolfo Madero, C.P. 07738 Ciudad de México, Mexico; jandraca@ipn.mx

3 Centro de Investigación en Materiales Avanzados SC, Unidad Monterrey-PIIT, 66628 Apodaca, Nuevo León, Mexico

* Correspondence: alfredo.morales@cimav.edu.mx (A.M.-S.); maceves@ieee.org (M.A.-M.); Tel.: +52-81-1156-0842 (A.M.-S.); +52-222-266-3100 (M.A.-M.)

Academic Editor: Paolo Minzioni
Received: 15 October 2016; Accepted: 8 December 2016; Published: 13 January 2017

Abstract: The photoluminescence characteristics of films consisting of Si nanocrystals either coated with or embedded into Spin on Glass (SOG) were studied. Si nanocrystals showing red or blue luminescence when suspended in alcohol solution were obtained from porous silicon films. These were then either deposited in Si substrates and coated with SOG, or mixed in an SOG solution that was later spun on Si substrates. Both types of films were thermally annealed at 1100 °C for three hours in N_2 atmosphere. Transmission electron microscopy measurements showed a mean diameter of 2.5 nm for the Si nanocrystals, as well as the presence of polycrystalline Si nanoagglomerates. These results were confirmed by X-ray diffraction studies, which revealed the (111), (220) and (311) Bragg peaks in Si nanocrystals. Fourier transform infrared spectroscopy studies showed that the coated films present higher chemical reactivity, promoting the formation of non-stoichiometric SiO_2, while the embedded films behave as a stoichiometric SiO_2 after the thermal annealing. The PL (photoluminescence) characterization showed that both embedded and coated films present emission dominated by the Quantum Confinement Effect before undergoing any thermal treatment. After annealing, the spectra were found to be modified only in the case of the coated films, due to the formation of defects in the nanocrystals/SiO_2 interface.

Keywords: Si-NCs (silicon nanocrystals); SOG; HRTEM (high resolution transmission electron microscopy); XRD (X-ray diffraction); FTIR (Fourier transform infrared spectroscopy); PL

1. Introduction

In the past, many efforts have been devoted to the fabrication of light emitting films that are compatible with silicon technology [1]. One of the proposed approaches is to use dielectric matrices with silicon nanocrystals (Si-NCs) or nano-agglomerates as active media. Among several other techniques, chemical methods have been used to fabricate such materials [2–10]. The origin of the photoluminescence (PL) of Si-NCs embedded into oxide films is still controversial [11], but there are two principal models commonly used to explain the emission mechanism. One is known as the Quantum Confinement Effect (QCE), in which the radiative process is carried out by electron-hole recombination in the Si-NCs; silicon nanocrystals below 5 nm show an effect of a quasi-direct bandgap due to the boundary conditions [6,8,12,13]. The second model proposes the formation of defect-states

at the Si-NCs/SiO_2 interface where radiative recombination occurs [10,14,15]. In the literature, there is enough evidence of SiO_2 defects with specific emissions that simultaneous experiments of luminescence and detection of defects have been done during the years to link them. Just to mention a few, electron paramagnetic resonance (EPR), time resolved photoluminescence, and tunable laser excitation are some of the techniques used [16–18].

Two main different emissive films of this kind have been proposed: those that produce centers with luminescent characteristics as they are synthetized; and films where Si-NCs are obtained separately from the dielectric matrix. In the first method, temperatures of around 1100 °C are needed to promote the nucleation and activation of radiative Si nanopoints, crystalline or not [3,4,19,20]. Examples of these materials are the silicon rich oxides obtained by chemical vapor deposition (CVD), Ionic implantation of Si in a dielectric matrix, and thermally treated chemical solutions [4,21–23]. These kind of silicon rich oxides show photoluminescence mainly in a range from 650 to 950 nm. However, if high energy is used to stimulate them, the range emission can be extended to the blue side of the electromagnetic spectrum. However, the high temperature annealing usually needed to promote the silicon-emissive center formation [3,4,19,20] complicates their potential incorporation in CMOS (complementary metal-oxide-semiconductor) integrated circuits.

On the other hand, Si-NCs obtained separately by a variety of techniques and mixed with SiO_2 solutions, such as Spin on Glass (SOG), have been of particular research interest because they are usually easy and low cost methods that do not need to be thermal treated to produce emissive films. In most of the cases, it has been reported that such films contain embedded Si-NCs embedded in the dielectric matrix. Their characteristic photoluminescence is rather on the blue side of the spectrum, varying with the diameter of the nanocrystals. Nevertheless, it has been reported that the emission depends on many factors, including the density of Si-NCs in the SOG, the way they are obtained and mixed, and the type and temperature used if they are annealed [24–27]. Then, despite the existence of several studies, much research is still to be done in order to fully understand the luminescence mechanisms, and the optimal technological conditions to obtain reliable highly emissive films.

In this work, in order to corroborate the chemical interaction between the Si-NCs and the SOG film, two different films are proposed: Si-NCs coated with a thin layer of SOG and Si-NCs embedded into the SOG film—hereafter, respectively referred to as "coated" and "embedded" films. Moreover, the coated and embedded films were studied with and without thermal annealing at 1100 °C to look deeply into its effects.

2. Experimental Details

The Porous Silicon (pSi) samples were prepared by anodic etching of epitaxial, <100>, *n*-type mono crystalline-silicon with an electrical resistivity between 2 Ω-cm and 0.025 Ω-cm. A solution mixture of hydrofluoric acid (44%), hydrogen peroxide (44%) and methanol (99.9%) with a volume ratio of 4:3:3 was used with a constant current of 40 mA. The pSi samples were obtained using a standard configuration of lateral anodizing in which samples were introduced at a rate of 4 mm/h into the solution [28]. Then, Si-NCs were obtained either scratching or milling the porous silicon layer. Scratching produces Si-NCs with an intense red emission, and milling produces blue PL emission [29]. The Si-NCs were then dispersed into isopropanol [$(CH_3)_2CHOH$)] to obtain colloidal solutions. The colloidal solutions were used to produce the coated or embedded test structures. Coated samples were fabricated by spraying the colloidal Si-NC solution onto Si substrates heated to 90 °C producing a layer of Si-NCs (~70 nm-thick). Then, these Si-NCs films were coated with a pure SOG solution (synthetized from a 99.99% Sigma Aldrich Tetraethyl orthosilicate, St. Louis, MO, USA). The SOG solution was spun at 3000 rpm for 50 s. The coated samples are schematized in Figure 1a.

The embedded films were obtained by mixing the colloidal solution with the SOG solution with a volume ratio of 3:1 (Si-NCs:SOG). Then, the SOG with embedded Si-NC solution was spun onto the silicon substrates at 3000 rpm for 50 s. These films are schematized in Figure 1b.

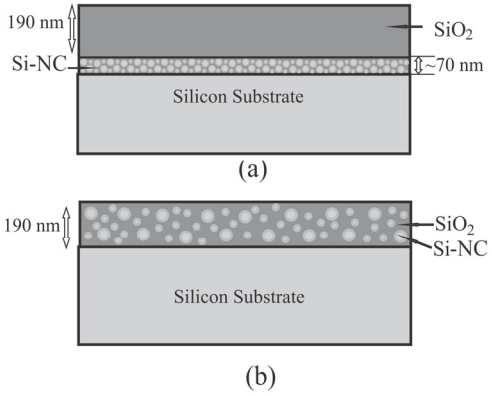

Figure 1. Schemes for: (**a**) coated; and (**b**) embedded films with **red** or **blue** Si-NCs (silicon nanocrystals).

Both coated and embedded films were heated at 150 °C to solidify the SOG and some of them were thermally annealed at 1100 °C in N_2 atmosphere for 3 h. The thicknesses of all films were measured with a Gaertner L117 null ellipsometer (Gaertner Scientific Corporation, Skokie, IL, USA) using a He-Ne incident laser of 632.8 nm wavelength and 2 mW of power. The coated and embedded films resulted with a thickness of ~190 nm and ~260 nm, respectively. The micro-structural properties of both coated and embedded films were studied by transmission electron microscopy (TEM; Tecnai F30, FEI Company, Hillsboro, OR, USA). Grazing incidence X-ray diffraction data were obtained with an X Pert PRO MRD diffractometer from PANalytical (Almelo, The Netherlands). The measurements were carried out with a Cu K_α (λ = 1.5418 Å) radiation as source. The grazing angle of the incident beam was fixed at 0.5° and the data acquisition angle was varied between 15° and 60° with a resolution of 0.05°, and with an acquisition time per angular step of 800 s. A computer controlled spectrometer Bruker Fourier transform infrared (FTIR) model V22 (Bruker Optics Inc., Billerica, MA, USA) was used to obtain the FTIR spectra of the films. The absorption spectra were acquired from 400 cm^{-1} to 4000 cm^{-1}. The photoluminescence measurements were carried out at room temperature for all samples using a computer controlled spectroflourometer model Flouromax-3 (Horiba, Kyoto, Japan). The samples were excited with a 300 nm wavelength and the emission spectra were recorded in the range of 370 nm to 1000 nm. A 300 nm band pass filter was used in the excitation monochromatic source and a 370 nm high pass filter was used for the PL detector.

3. Results and Discussion

3.1. Structural Properties

3.1.1. Transmission Electron Microscopy

Figure 2 shows the cross section TEM images of coated films with red light-emitting Si-NCs before (A) and after (B) thermal annealing. Before annealing, a clear frontier between the crystalline Si-NCs and amorphous SOG layers can be observed. Conversely, the frontier between the amorphous and the crystalline regions is practically lost after thermal annealing. Furthermore, it is then possible to observe some amorphous barriers between the Si-NCs (white circle in the Figure 2B). This is probably because the thermal treatment promotes the flow of the SOG through the layer of the Si-NCs. The insets of Figure 2B(b) shows an FFT (Fast Fourier Transform) performed to the TEM images (Figure 2B(a)) in order to determine the distance between atomic layers of Si-NCs. The nanocrystal lattice spacing in high resolution transmission electron microscopy (HRTEM) images was estimated using the digital micrograph software (version 3.1.1, Gatan Inc., Pleasanton, CA, USA) to identify the orientation of the crystalline planes. The distances obtained correspond to the face-centered cubic lattice of crystalline silicon (joint committee on powder diffraction standards (JCPDS) #27-1402) (see inset Figure 2B(d)).

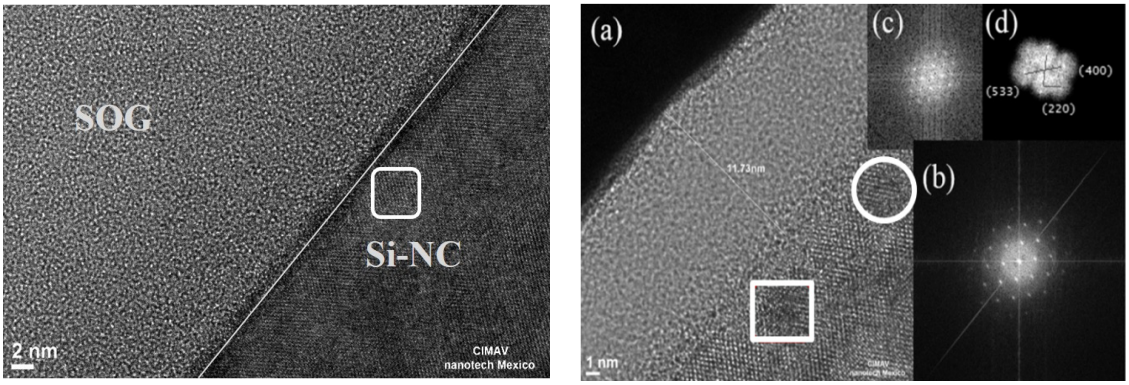

(**A**) (**B**)

Figure 2. Cross-section TEM (transmission electron microscopy) images of coated films with **red** Si-NCs before (**A**) and after (**B**) thermal annealing at 1100 °C for 3 h in N_2 atmosphere. In both images, the **white** square marks the area of analysis where there are Si-NCs. The insets of (**B**) are: (**a**) cross-section TEM images; (**b**) FFT (Fast Fourier Transform); (**c**) the specific pattern of the **white** square area; and (**d**) the electrons diffraction planes of the **white** square area. The **white** circle in the Figure 2B shows a zone where the SOG (Spin on Glass) flowed around the Si-NC after annealing.

Due to the nature of the coated films, it is not possible to observe the shape of Si-NCs. However, in the case of films with embedded red light-emitting Si-NCs (Figure 3A), it is possible to observe nearly spherical particles, as typically produced by the electrochemical technique [28]. The nanocrystals' diameter ranges from 1.5 nm to 4.5 nm with a mean size of 2.5 nm. In addition, a variety of crystalline planes corresponding to polycrystalline agglomerates was discovered, as observed in the inset Figure 3A(d).

In the case of embedded films made with blue light-emitting Si-NCs, these cannot be clearly observed with the naked eye in the TEM images (Figure 3B(a)), making it difficult to select the area to perform the FFT analysis. However, some diffraction patterns can be observed after processing the TEM images, as shown in the inset Figure 3B(d). These diffraction patterns indicate crystalline silicon with cubic structure. This was confirmed with the X-ray measurements.

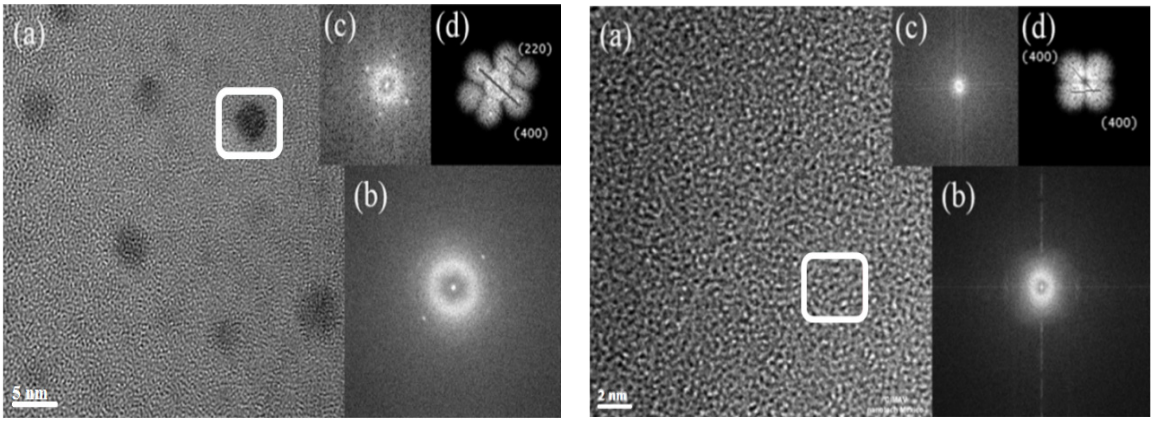

(**A**) (**B**)

Figure 3. Cross-section TEM images of embedded films with **red** (**A**) and **blue** (**B**) Si-NCs, after thermal annealing at 1100 °C for 3 h in N_2 atmosphere. In both images, the **white** square marks the area of analysis where there is a Si-NCs. The insets are: (**a**) the cross-section TEM images; (**b**) FFT; (**c**) the specific pattern of the **white** square area; and (**d**) the electrons' diffraction planes of the **white** square areas, for each image.

3.1.2. Grazing Incidence X-Ray Diffraction

Figure 4 shows the X-ray diffraction patterns of coated (a) and embedded films (b) before and after annealing. A well-defined main peak is observed at 28.4°, as well as peaks with lower intensities at 47.3° and 56.1°, which respectively correspond to (111), (220), and (311) Bragg peaks for silicon. These peaks match very well the PDF JCPDS #27-1402 values for cubic crystalline structure of silicon. The diffraction plane corresponds to a face centered cubic lattice as the obtained by the TEM analysis (Figures 2 and 3). These peaks indicate that the coated and embedded films contain Si-NCs with a face centered cubic lattice structure.

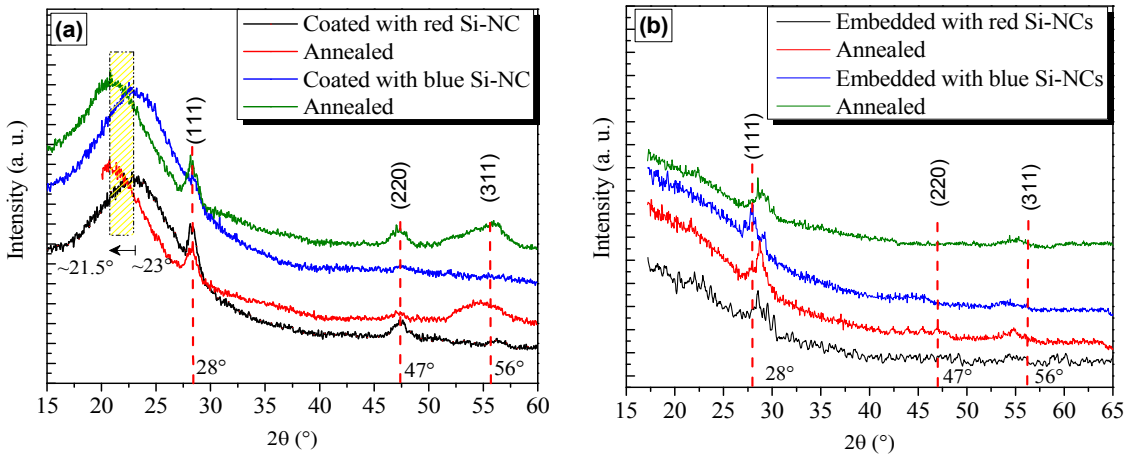

Figure 4. Grazing incidence XRD (X-ray diffraction) (0.5°) patterns from coated (**a**) and embedded films; (**b**) with **red** and **blue** light-emitting Si-NCs, before and after annealing at 1100 °C for 3 h in N_2 atmosphere.

As observed in Figure 4a, a wide peak centered at ~23° can be seen in as-deposited samples, which shifts to a lower angle of 21.5° after thermal annealing for coated films with both red and blue Si-NCs. This shift has been associated with the formation of amorphous silicon oxide (a-SiO_2) due to spinoidal decomposition [30]. Therefore, the structural units of the SOG, which can be described by the different tetrahedral units $SiO_{4-x}Si_x$ with $n = 0-4$, gradually transform into well-defined SiO_4 and Si-Si_4 tetrahedral structures [23,24]. This transformation, only observed in the coated films, agrees with the TEM observation of the SOG flowing into the Si-NCs layer after thermal annealing.

3.1.3. Fourier Transform Infrared Spectroscopy

Figure 5 shows the typical FTIR spectra before and after annealing of a pure SOG film (a), embedded films (b), and coated films (c) containing red light-emitting Si-NCs. The same behavior was observed in coated and embedded films with blue light-emitting Si-NCs.

The typical IR (infrared) vibration modes from silicon oxide films [31,32] at 1078 cm^{-1} (Si-O-Si stretching), 800 cm^{-1} (O-Si-O bending), and 457 cm^{-1} (Si-O-Si rocking) can be observed in all of the cases. All the absorption spectra show a peak at 1400 cm^{-1} due to the Si-CH_2 stretching bonds, as well as some other peaks related to vibration modes associated with hydrogen bonds at 935 cm^{-1} (Si-OH stretching) and >3200 (H_2O) cm^{-1}. The latter decreases in intensity or disappears after the thermal annealing [31,32]. It is noticeable that both before and after annealing, the IR spectra of the pure SOG film are similar to the IR spectra obtained from the coated and embedded films with Si-NCs (Figure 5b,c).

Figure 6 shows the IR peak related to the Si-O-Si asymmetric stretching mode deconvoluted in their longitudinal (LO) and transversal (TO) modes of the different samples, in order to qualitatively assess the structural changes produced by the thermal annealing [7,33–35].

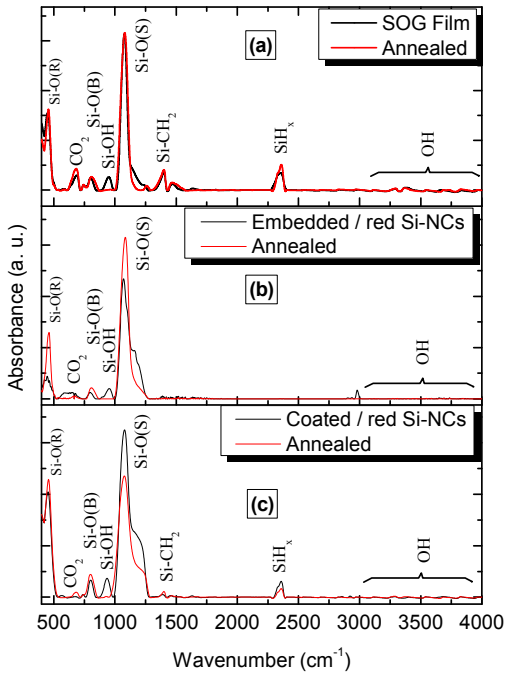

Figure 5. (Color Online) FTIR (Fourier transform infrared) spectra before and after annealing at 1100 °C for 3 h in N_2 atmosphere of pure SOG film (**a**); embedded (**b**); and coated (**c**) films fabricated with **red** Si-NCs.

In all of the spectra in Figure 6, it is possible to see the stretching peak (at ~1078 cm^{-1}) and the asymmetric stretching peak (from 1100 cm^{-1} to 1200 cm^{-1}). Notice that these spectra show a shift to lower or higher wavenumbers depending on its structure or composition after annealing.

The stretching infrared (IR) peak observed in coated samples with red and blue Si-NCs shifts towards a lower wavenumber after thermal annealing, as observed in Figure 6a,b, respectively. However, this IR band shifts towards the opposite direction for the embedded red and blue Si-NCs films, as observed in Figure 6c,d, respectively. A deconvolution of the IR stretching peak (symmetric and asymmetric) in the LO and TO modes shows a change in the full width at a half maximum (FWHM) associated with the formation of amorphous phases of SiO_2 (peak at ~1025 cm^{-1}) in the Si-NCs/SOG interface after thermal annealing. This is an indication of a possible combination of non-stoichiometric and stoichiometric SiO_2 [7,36]. The Si-NCs could react with the oxygen atoms of the SOG due to the silicon atoms presenting a higher probability of having oxygen neighboring atoms, forming Si=O related bonds [14]. This is confirmed by the shift of about 16.4 cm^{-1} and 13.7 cm^{-1} to lower wavenumbers of the stretching Si-O-Si peak for each coated film, as observed in Figure 6a,b. In addition, the observed broadening of the IR stretching peak could be related to a strain between the Si-NCs and the SiO_2-based SOG film, producing the formation of a high defect density after the thermal annealing in N_2 atmosphere [37].

On the other hand, the shift of the IR stretching peak found in the embedded Si-NCs towards higher wavenumbers after thermal annealing could be related to the formation of a stoichiometric and dense film (shifts of 15.9 cm^{-1} and 16.2 cm^{-1} for red and blue embedded Si-NCs film, respectively). Therefore, a structural rearrangement occurs in these films due to the thermal annealing, improving the stoichiometry because of the phase separation between the Si and SiO_2 [34,38]. In addition, the decrease in the intensity from the IR asymmetric stretching peak (found between 1100 cm^{-1} and 1200 cm^{-1}), which can be seen in the decrease of the longitudinal and transversal optical modes, denotes stress relief in the Si-NCs/SOG interface.

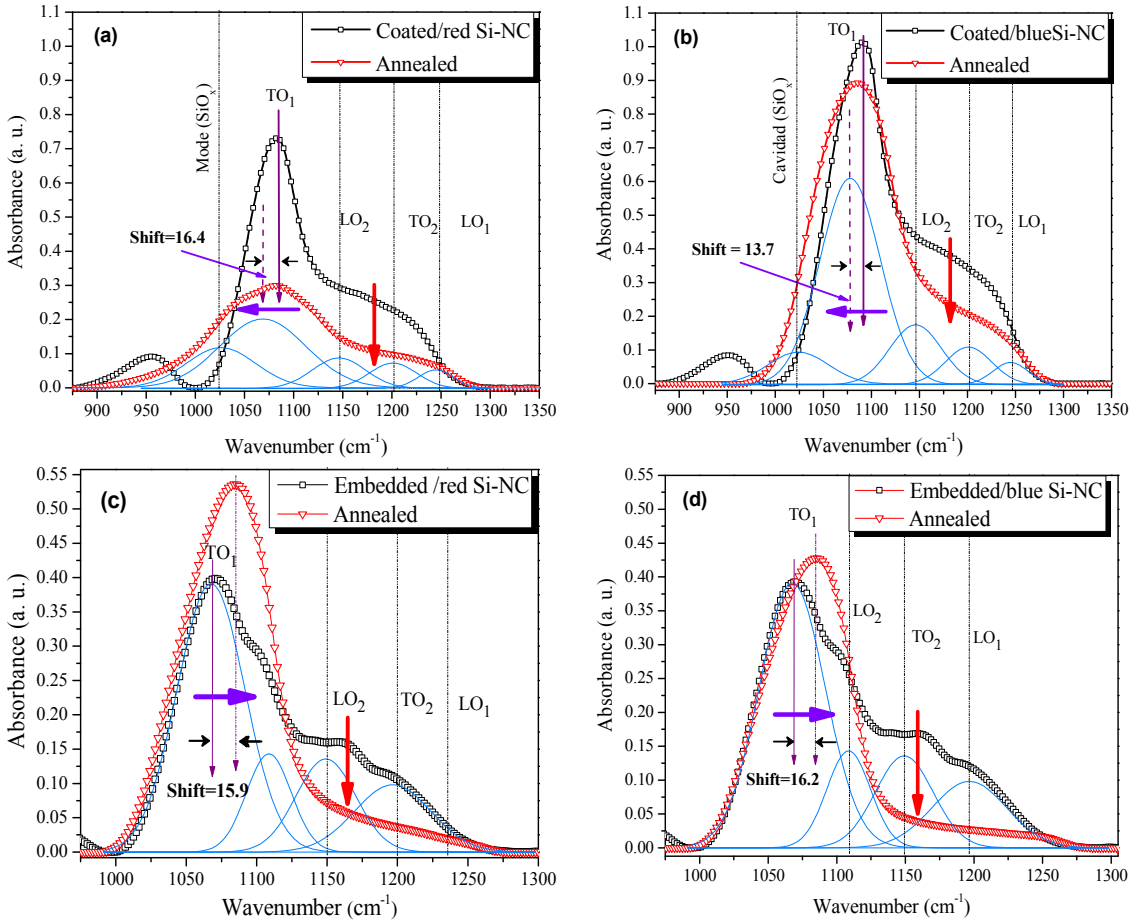

Figure 6. (Color Online) FTIR spectra of coated and embedded films before and after annealing at 1100 °C for 3 h in N_2 atmosphere. (**a**,**b**) are the IR (infrared) spectra of coated films with **red** and **blue** Si-NCs, respectively; (**c**,**d**) are the IR spectra of embedded films with **red** and **blue** Si-NCs, respectively.

3.2. Photoluminescence Properties

Si-NCs obtained through porous silicon samples exhibit a typical strong red PL emission with a quasi-Gaussian curve [31], which is usually attributed to the quantum confinement effect [1,6]. The PL spectra obtained from the Si-NCs-based colloidal solutions for this work are shown in Figure 7a. The PL spectrum of the red Si-NC colloidal solution has a main peak at around 639 nm (which is similar to that of pSi layers; not shown), and a lower intensity secondary PL peak at 400 nm. As observed in Figure 7a, the PL spectrum of the isopropanol solution without Si-NCs also exhibits peaks at about 415 nm, but its intensity is very low as compared to the PL from samples with them.

The blue Si-NC colloidal solution exhibits an intense PL band at ~400 nm and an additional PL band of lower intensity around 753 nm. The intense PL band centered at 400 nm is mainly associated with the blue Si-NCs, since the isopropanol luminescence is known to be too low. These PL emission bands have been reported before [8,24,25].

Figure 7b shows the PL spectra of the coated red and blue Si-NC films before thermal annealing. Coated red Si-NCs show a broad PL band with a maximum peak at ~650 nm and a less intense band at ~415 nm, while the coated blue Si-NC films emit an intense PL band with the main peak at ~410 nm and a very small secondary peak at ~800 nm.

The PL emission of the red Si-NCs was related to their diameter distribution and their energy bandgap. Assuming a nearly spherical configuration of the nanocrystals, calculations of the energy gap were made using the mathematical expression [39]:

$$E_{eh} = 1.1eV + h^2/(8 * m_e R^2) + h^2/(8 * m_h R^2), \quad (1)$$

where m_e and m_h are the effective masses of the electron and hole, respectively; R is the radius of the nanocrystals; and h is Planck's constant. According to Equation (1), considering an $m_e = 1.08m_0$, and a $m_h = 0.56m_0$, where $m_0 = 9.11 \times 10^{-31}$ kg is the free electron rest mass [40], the estimated diameter of the Si-NCs producing a PL emission at 650 nm is 2.3 nm. This is consistent with the diameter distribution obtained from HRTEM images for red Si-NCs, which is between 1.5 nm to 4.5 nm, with a mean of 2.5 nm. This supports the conclusion stating that the emission of red Si-NCs is mainly due to QCE. A similar result is obtained from blue colloidal solution and coated blue Si-NCs films before the thermal annealing. Using Equation (1) and the PL spectrum of the blue Si-NCs, the nanocrystals' diameter ranges from 1.3 nm to 1.9 nm with a mean of 1.4 nm. Unfortunately, the observation of Si-NCs of less than 1.5 nm is not possible in the available HRTEM. Nevertheless, the presence of the blue Si-NCs was confirmed by XRD. Moreover, the PL emission from the colloidal solution is similar to the one observed in the coated films. Therefore, the light emission mechanism in these coated films is likely related to QCE as well.

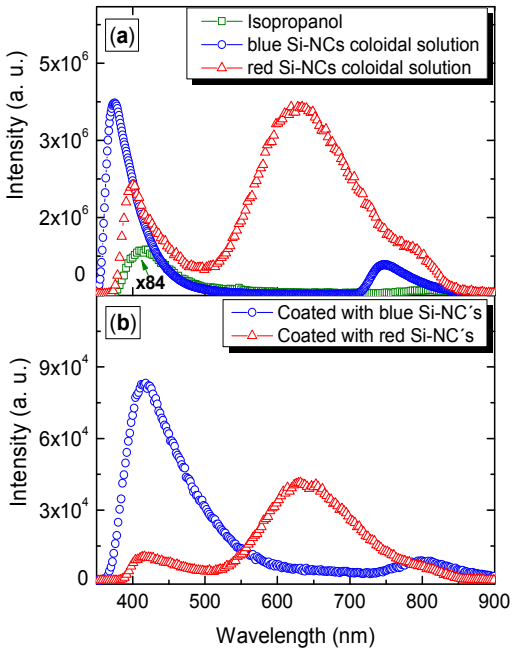

Figure 7. (Color Online) PL (Photoluminescence) spectra obtained at room temperature from colloidal solution (**a**); and from coated films with **red** and **blue** Si-NCs without annealing (**b**).

As observed in Figure 8, after thermal annealing, the PL emission spectra from both red and blue Si-NCs coated films are broadened. It now presents a wavelength range from ~400 nm to 850 nm. This behavior indicates that, regardless of having different Si-NCs, similar emission mechanisms take place in both samples after the thermal annealing, as discussed in a previous report [29].

The thermal annealing produces important effects in the response of the material. In particular, it results in an increase of the radiative surface states density at the Si-NCs/SiO_2 interface [41,42], as discussed in the previous sections. The shift of the Si-O-Si stretching mode to a lower wavenumber indicates a phase change towards an amorphous (non-stoichiometric silicon oxide) and porous structure [33–37]. This could be related to the formation of a SiO_x shell around silicon nanocrystals formed by a wide variety of Si-O bond defects. In a recent publication, Vaccaro et al. have corroborated the formation of a core shell structure with a crystalline core surrounded by an interface mainly composed by Si_3O defects [43].

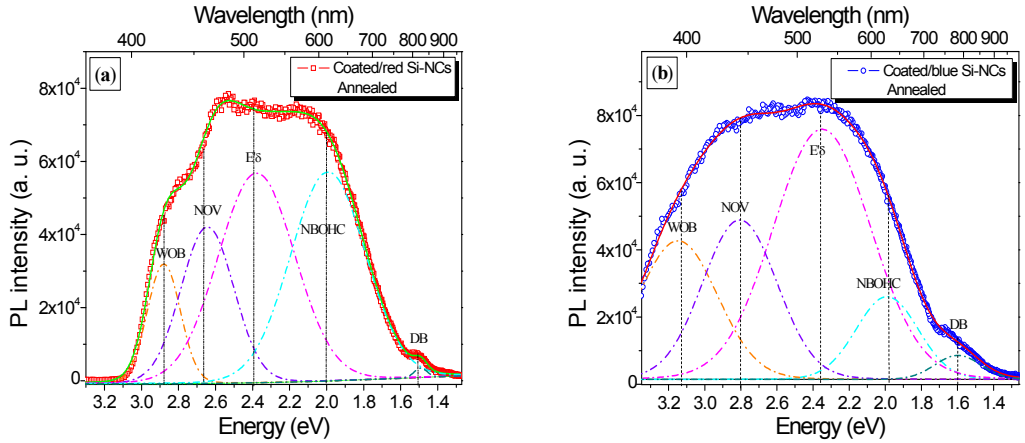

Figure 8. (Color Online) PL emission of coated films with **red** (**a**) and **blue** (**b**) Si-NCs after annealing at 1100 °C in N_2. Compared to Figure 7, these spectra are wider, and both shift towards the **blue-green** region of the visible spectrum.

The thermal annealing also appears to cause the loss of the H-passivated characteristics of the Si-NCs, modifying its configuration into an oxygen-passivated surface. This is corroborated by the FTIR results (Figure 5c). Therefore, it is likely that part of the emission remains due to recombination inside the nanocrystals, but oxygen defects also contribute to the broadening of the range of emission in both types of coated films.

The broad PL spectra were decomposed in Gaussian curves centered in the position of reported Si-O defect emissions, as shown in Figure 8a,b. As a result, PL bands at about 3.02 eV, 2.73 eV, 2.37 eV,1.99 eV, and 1.55 eV, were identified, which are respectively related to: weak-oxygen bond (WOB) [44], Neutral Oxygen Vacancy (NOV) [45], E'_δ center [46], non-bridging oxygen hole center (NBOHC) [18,47,48] and dangling bonds (DB) [49]. It was found that NBOHC and E'_δ centers are the dominant radiative defects for each of the coated films. The band around 2.7 eV has also been related to a twofold coordinated Si [16,17]. However, recently, the red emission around 1.9 eV has been related to Si_3O, and so the main contribution can be also ascribed to this defect [43]. These results agree with a previous report in which the main emission mechanism was associated to Si-O defects [29].

Figure 9 shows the PL emission spectra of embedded films with red (a) and blue (b) Si-NCs before and after thermal annealing. It is worth mentioning that any PL emission is observed when a Si-NCs:SOG volume ratio is lower than 3:1. As can be seen, the PL spectra are different than those observed in coated Si-NCs. Even though coated and embedded films were fabricated using the same Si-NCs, their respective spectrum has noticeable alterations. Before thermal annealing, the wavelength range of PL emission of both coated and embedded Si-NCs films are similar. However, after annealing, the emission of the embedded films shows practically no variation, contrary to the coated films.

The PL spectrum obtained from the embedded films with red Si-NCs presents a peak at ~715 nm, and a more intense one at ~410 nm, which is related to the SOG PL emission, as observed in Figure 9a. The embedded films with blue Si-NCs exhibit a maximum PL peak at ~430 nm, and a less intense one at ~850 nm, as shown in Figure 9b. The PL emission observed in embedded films with both red and blue Si-NCs before thermal annealing is similar to that observed in the colloidal solutions (Figure 7a). Since the SOG around the Si-NCs is not chemically bonded to them, the embedded film emission is ascribed to the quantum confinement mechanism, as proposed by other authors for similar films [25,50].

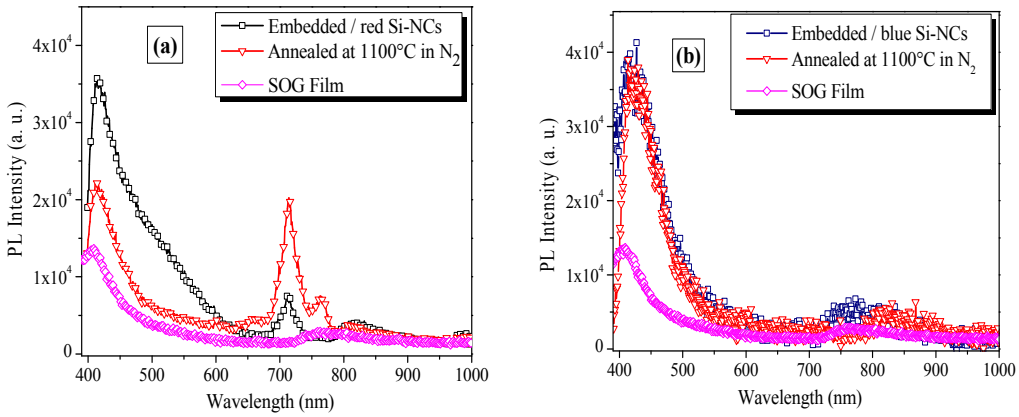

Figure 9. (Color Online) PL emission spectra of embedded films with **red** (**a**) and **blue** Si-NCs (**b**) before and after annealing at 1100 °C in N_2 atmosphere. PL spectra from pure SOG films are included.

When thermal annealing is applied to these embedded films, it is clear that the PL emission changes in intensity, but not in shape, as shown in Figure 9a. Because of this, the PL of the embedded films (with both red and blue Si-NCs) can be attributed to the quantum confinement effect before and after thermal annealing. Then, we can assume that there is no nitridation effect or any radiative defect formation in the Si-NC/SiO_2 interface for embedded films. This is confirmed by the absence of emission bands related to Si-O defects [23]. It is possible that thermal annealing in nitrogen passivates the non-radiative centers around the Si-NCs, showing only the PL emission from Si-NCs [4,19]. This passivation effect increases the PL intensity from the red Si-NCs, but reduces that from the blue ones. This is also corroborated by the shift of the IR stretching peak towards higher wavenumbers and the reduced intensity of the peak at 1200 cm^{-1} after thermal annealing, forming a well-defined shoulder in the asymmetric stretching peak (Figure 6c,d). This behavior allows for arguing that the PL emission of the embedded films is mainly due to the contribution of Si-NCs.

It is well known that the films with Si-NCs obtained externally to the dielectric film are highly dependent on the way they were mixed with the SOG solution. The experimental evidence presented here shows that when the Si-NCs are embedded in the dielectric matrix, the interfaces between the Si and the SiO_2 are well defined, and even after high temperature treatments, there are no chemical interactions between the silicon and its surroundings. This is corroborated by other authors who observed a quenching of PL after thermal annealing [27].

However, when the Si-NCs are coated (as opposed to embedded) by the SOG, and then annealed, the SiO_2 flows around the Si-NCs, promoting the formation of silicon-oxide bonds. Then, a sintered type of core elemental silicon surrounded by a shell of non-stoichiometric oxide is obtained. The off-stoichiometric oxide contains silicon defects, which are luminescent under excitation. In this paper, after 1100 °C annealing, the samples show an emission shift toward a range around 500 nm regardless of the Si-NC size. However, other emission ranges can be obtained when the same type of samples are subjected to different annealing conditions [29]. Therefore, in order to obtain efficient Si light emitters using nanocrystals externally acquired, the results indicate that it is better to cover them with the dielectric matrix and apply a thermal treatment.

4. Conclusions

Porous silicon obtained by electrochemical methods has been used to produce colloidal solutions with silicon nanocrystals that show red or blue PL emission. These colloidal solutions were used to fabricate SOG-coated and embedded films. In both solutions, Si-NCs were studied using TEM and XRD techniques. The size of the red light-emitting Si-NCs as observed through TEM agrees with PL results. From FTIR, a notable difference between coated and embedded films was found, mainly in

the Si-O stretching peak, which shifts to show non-stoichiometric characteristics for coated films and stoichiometric SiO_2 for embedded films.

From PL measurements, it was found that the colloidal solutions, and as-deposited coated and embedded films, show an intense PL emission, which was related to the nanocrystal sizes (QCE). When a thermal annealing process is carried out, the PL of embedded films does not change, and the quantum confinement effect remains as the emission mechanism. However, coated films with both red and blue Si-NCs do change their PL spectrum towards the blue-green region after annealing, demonstrating that a chemical activity occurs only in the covered films after sintering at 1100 °C. A correlation between photoluminescence and the FTIR results shows that the Si-NCs interface evolves, developing Si-O defects for such types of films. The new emission band is ascribed to a wide variety of Si-O related defects formed at the Si-NC/SiO_2 interface. The analysis of the emission indicated that a high density of the radiative NBOHC and E'_δ center dominates the PL emission from coated films after annealing.

Acknowledgments: The authors are thankful to Consejo Nacional de Ciencia y Tecnología (CONACYT) for the economic support and Pablo Alarcon for his help during the sample preparation.

Author Contributions: This paper is the result of O.C.-M.'s PhD work, who was under the supervision of M.A.-M. M.A.V.-A. and A.A.G.-F. were mostly involved in the setup of the experiments, also in the redaction of the paper. J.A.A.-A. was responsible for the X-ray measurements and interpretation of the data. A.M.-S. performed the TEM studies and reviewed the manuscript."

Conflicts of Interest: The authors declare no conflict of interest.

References

1. Lehmann, V.; Gösele, U. Porous silicon formation: A quantum wire effect. *Appl. Phys. Lett.* **1991**, *58*, 856–858. [CrossRef]
2. Doğan, İ.; Kramer, N.J.; Westermann, R.H.; Dohnalová, K.; Smets, A.H.; Verheijen, M.A.; Gregorkiewicz, T.; van de Sanden, M.C. Ultrahigh throughput plasma processing of free standing silicon nanocrystals with lognormal size distribution. *J. Appl. Phys.* **2013**, *113*. [CrossRef]
3. Bolduc, M.; Genard, G.; Yedji, M.; Barba, D.; Martin, F.; Terwagne, G.; Ross, G.G. Influence of nitrogen on the growth and luminescence of silicon nanocrystals embedded in silica. *J. Appl. Phys.* **2009**, *105*. [CrossRef]
4. Quiroga-González, E.; Bensch, W.; Aceves-Mijares, M.; Yu, Z.; López-Estopier, R.; Monfil-Leyva, K. On the photoluminescence of multilayer arrays of silicon rich oxide with high silicon content prepared by low pressure chemical vapor deposition. *Thin Solid Films* **2011**, *519*, 8030–8036. [CrossRef]
5. Fauchet, P.M.; Ruan, J.; Chen, H.; Pavesi, L.; Dal Negro, L.; Cazzaneli, M.; Elliman, R.G.; Smith, N.; Samoc, M.; Luther-Davies, B. Optical gain in different silicon nanocrystal systems. *Opt. Mater.* **2005**, *27*, 745–749. [CrossRef]
6. Ledoux, G.; Gong, J.; Huisken, F.; Guillois, O.; Reynaud, C. Photoluminescence of size-separated silicon nanocrystals: Confirmation of quantum confinement. *Appl. Phys. Lett.* **2002**, *80*, 4834–4836. [CrossRef]
7. Ray, M.; Hossain, S.M.; Klie, R.F.; Banerjee, K.; Ghosh, S. Free standing luminescent silicon quantum dots: evidence of quantum confinement and defect related transitions. *Nanotechnology* **2010**, *21*. [CrossRef] [PubMed]
8. Valenta, J.; Janda, P.; Dohnalová, K.; Nižňansky, D.; Vácha, F.; Linnros, J. Colloidal suspensions of silicon nanocrystals: from single nanocrystals to photonic structures. *Opt. Mater.* **2005**, *27*, 1046–1049. [CrossRef]
9. Švrček, V.; Rehspringer, J.L.; Slaoui, A.; Pivac, B.; Muller, J.C. Clustering/declustering of silicon nanocrystals in spin-on glass solutions. *Semicond. Sci. Technol.* **2005**, *20*, 314–319. [CrossRef]
10. Chen, X.Y.; Lu, Y.F.; Wu, Y.H.; Cho, B.J.; Liu, M.H.; Dai, D.Y.; Song, W.D. Mechanisms of photoluminescence from silicon nanocrystals formed by pulsed-laser deposition in argon and oxygen ambient. *J. Appl. Phys.* **2003**, *93*, 6311–6319. [CrossRef]
11. Ali, A.M.; Kobayashi, H.; Inokuma, T.; Al-Hajry, A. Morphological, luminescence and structural properties of nanocrystalline silicon thin films. *Mater. Res. Bull.* **2013**, *48*, 1027–1033. [CrossRef]

12. Godefroo, S.; Hayne, M.; Jivanescu, M.; Stesmans, A.; Zacharias, M.; Lebedev, O.I.; Van Tendeloo, G.; Moshchalkov, V.V. Classification and control of the origin of photoluminescence from Si nanocrystals. *Nat. Nanotechnol.* **2008**, *3*, 174–178. [CrossRef] [PubMed]
13. Dohnalová, K.; Poddubny, A.N.; Prokofiev, A.A.; De Boer, W.D.; Umesh, C.P.; Paulusse, J.M.; Zuilhof, H.; Gregorkiewicz, T. Surface brightens up Si quantum dots: Direct bandgap-like size-tunable emission. *Light Sci. Appl.* **2013**, *2*. [CrossRef]
14. Wolkin, M.V.; Jorne, J.; Fauchet, P.M.; Allan, G.; Delerue, C. Electronic States and Luminescence in Porous Silicon Quantum Dots: The Role of Oxygen. *Phys. Rev. Lett.* **1999**, *82*, 197–200. [CrossRef]
15. Dohnalová, K.; Gregorkiewicz, T.; Kůsová, K. Silicon quantum dots: Surface matters. *J. Phys. Condens. Matter* **2014**, *26*. [CrossRef] [PubMed]
16. Skuja, L. Optically active oxygen-deficiency-related centers in amorphous silicon dioxide. *J. Non-Cryst. Solids* **1998**, *239*, 16–48. [CrossRef]
17. Spallino, L.; Vaccaro, L.; Sciortino, L.; Agnello, S.; Buscarino, G.; Cannas, M.; Gelardi, F.M. Visible-ultraviolet vibronic emission of silica nanoparticles. *Phys. Chem. Chem. Phys.* **2014**, *16*, 22028–22034. [CrossRef] [PubMed]
18. Vaccaro, L.A.; Cannas, M.A.; Boscaino, R.O. Luminescence features of nonbridging oxygen hole centres in silica probed by site-selective excitation with tunable laser. *Solid State Commun.* **2008**, *146*, 148–151. [CrossRef]
19. Carrada, M.; Wellner, A.; Paillard, V.; Bonafos, C.; Coffin, H.; Claverie, A. Photoluminescence of Si nanocrystal memory devices obtained by ion beam synthesis. *Appl. Phys. Lett.* **2005**, *87*. [CrossRef]
20. Limpens, R.; Lesage, A.; Fujii, M.; Gregorkiewicz, T. Size confinement of Si nanocrystals in multinanolayer structures. *Sci. Rep.* **2015**, *5*. [CrossRef] [PubMed]
21. Aceves-Mijares, M.; Espinosa-Torres, N.D.; Flores-Gracia, F.; González-Fernández, A.A.; López-Estopier, R.; Román-López, S.; Pedraza, G.; Domínguez, C.; Morales, A.; Falcony, C. Composition and emission characterization and computational simulation of silicon rich oxide films obtained by LPCVD. *Surf. Interface Anal.* **2014**, *46*, 216–223. [CrossRef]
22. Hessel, C.M.; Summers, M.A.; Meldrum, A.; Malac, M.; Veinot, J.G. Direct Patterning, Conformal Coating, and Erbium Doping of Luminescent nc-Si/SiO_2 Thin Films from Solution Processable Hydrogen Silsesquioxane. *Adv. Mater.* **2007**, *19*, 3513–3516. [CrossRef]
23. Lin, G.R.; Lin, C.J.; Lin, C.K.; Chou, L.J.; Chueh, Y.L. Oxygen defect and Si nanocrystal dependent white-light and near-infrared electroluminescence of Si-implanted and plasma-enhanced chemical-vapor deposition-grown Si-rich SiO_2. *J. Appl. Phys.* **2005**, *97*. [CrossRef]
24. Švrček, V.; Sasaki, T.; Shimizu, Y.; Koshizaki, N. Colloidal blue and red luminescent silicon nanocrystals and their elaboration in pure and doped spin on glasses. *Phys. E Low Dimens. Syst. Nanostruct.* **2007**, *40*, 293–296. [CrossRef]
25. Švrček, V.; Sasaki, T.; Shimizu, Y.; Koshizaki, N. Silicon nanocrystals formed by pulsed laser-induced fragmentation of electrochemically etched Si micrograins. *Chem. Phys. Lett.* **2006**, *429*, 483–487. [CrossRef]
26. Svrcek, V.; Sasaki, T.; Shimizu, Y.; Koshizaki, N. Blue luminescent silicon nanocrystals prepared by nanosecond laser ablation and stabilized in electronically compatible spin on glasses. *J. Appl. Phys.* **2008**, *103*. [CrossRef]
27. Švrček, V.; Slaoui, A.; Rehspringer, J.L.; Muller, J.C. Photoluminescence studies from silicon nanocrystals embedded in spin on glass thin films. *J. Lumin.* **2003**, *101*, 269–274. [CrossRef]
28. Nayfeh, M.H.; Rao, S.; Nayfeh, O.M.; Smith, A.; Therrien, J. UV Photodetectors with Thin-Film Si Nanoparticle Active Medium. *IEEE Trans. Nanotechnol.* **2005**, *4*, 660–668. [CrossRef]
29. Cortazar, O.; Vasquez-A, M.A.; Aceves-Mijares, M. Effect of the Annealing Atmosphere and Temperature on the Photoluminescence of Si Nanocrystal Films Covered with Spin-On Glass. *J. Nanoelectron. Optoelectron.* **2015**, *10*, 93–98. [CrossRef]
30. Comedi, D.; Zalloum, O.H.; Irving, E.A.; Wojcik, J.; Roschuk, T.; Flynn, M.J.; Mascher, P. X-ray-diffraction study of crystalline Si nanocluster formation in annealed silicon-rich silicon oxides. *J. Appl. Phys.* **2006**, *99*. [CrossRef]
31. Vásquez-A., M.A.; Águila Rodríguez, G.; García-Salgado, G.; Romero-Paredes, G.; Peña-Sierra, R. FTIR and photoluminescence studies of porous silicon layers oxidized in controlled water vapor conditions. *Rev. Mex. Fís.* **2007**, *53*, 431–435.

32. Lau, W.S. *Infrared Characterization for Microelectronics*; World Scientific: Singapore, 1999.
33. Chou, J.S.; Lee, S.C. Effect of porosity on infrared-absorption spectra of silicon dioxide. *J. Appl. Phys.* **1995**, *77*, 1805–1807. [CrossRef]
34. Hayashi, S.; Tanimoto, S.; Yamamoto, K. Analysis of surface oxides of gas-evaporated Si small particles with infrared spectroscopy, high-resolution electron microscopy, and X-ray photoemission spectroscopy. *J. Appl. Phys.* **1990**, *68*, 5300–5308. [CrossRef]
35. Daldosso, N.; Das, G.; Larcheri, S.; Mariotto, G.; Dalba, G.; Pavesi, L.; Irrera, A.; Priolo, F.; Iacona, F.; Rocca, F. Silicon nanocrystal formation in annealed silicon-rich silicon oxide films prepared by plasma enhanced chemical vapor deposition. *J. Appl. Phys.* **2007**, *101*. [CrossRef]
36. Borghesi, A.; Piaggi, A.; Sassella, A.; Stella, A.; Pivac, B. Infrared study of oxygen precipitate composition in silicon. *Phys. Rev. B* **1992**, *46*, 4123–4127. [CrossRef]
37. Chayani, M.; Caquineau, H.; Despax, B.; Bandet, J.; Berjoan, R. Variations in the physico-chemical properties of near-stoichiometric silica deposited from SiH_4–N_2O and SiH_4–N_2O–He radiofrequency discharges. *Thin Solid Films* **2005**, *471*, 53–62. [CrossRef]
38. Alayo, M.I.; Pereyra, I.; Scopel, W.L.; Fantini, M.C. On the nitrogen and oxygen incorporation in plasma-enhanced chemical vapor deposition (PECVD) SiO_xN_y films. *Thin Solid Films* **2002**, *402*, 154–161. [CrossRef]
39. Kumar, V. *Nanosilicon*; Elsevier: Amsterdam, The Netherlands, 2011.
40. Neamen, D.A. *Semiconductor Physics and Devices*; McGraw-Hill Higher Education: New York, NY, USA, 2003.
41. Dinh, L.N.; Chase, L.L.; Balooch, M.; Siekhaus, W.J.; Wooten, F. Optical properties of passivated Si nanocrystals and SiO_x nanostructures. *Phys. Rev. B* **1996**, *54*, 5029–5037. [CrossRef]
42. Nishikawa, H.; Watanabe, E.; Ito, D.; Sakurai, Y.; Nagasawa, K.; Ohki, Y. Visible photoluminescence from Si clusters in γ-irradiated amorphous SiO_2. *J. Appl. Phys.* **1996**, *80*, 3513–3517. [CrossRef]
43. Vaccaro, L.; Popescu, R.; Messina, F.; Camarda, P.; Schneider, R.; Gerthsen, D.; Gelardi, F.M.; Cannas, M. Self-limiting and complete oxidation of silicon nanostructures produced by laser ablation in water. *J. Appl. Phys.* **2016**, *120*. [CrossRef]
44. Nishikawa, H.; Watanabe, E.; Ito, D.; Takiyama, M.; Ieki, A.; Ohki, Y. Photoluminescence study of defects in ion-implanted thermal SiO_2 films. *J. Appl. Phys.* **1995**, *78*, 842–846. [CrossRef]
45. Zhao, X.; Schoenfeld, O.; Kusano, J.I.; Aoyagi, Y.; Sugano, T. Observation of Direct Transitions in Silicon Nanocrystallites. *Jpn. J. Appl. Phys.* **1994**, *33*, L899–L901. [CrossRef]
46. Chou, S.T.; Tsai, J.H.; Sheu, B.C. The photoluminescence in Si^+-implanted SiO_2 films with rapid thermal anneal. *J. Appl. Phys.* **1998**, *83*, 5394–5398. [CrossRef]
47. Nishikawa, H.; Nakamura, R.; Tohmon, R.; Ohki, Y.; Sakurai, Y.; Nagasawa, K.; Hama, Y. Generation mechanism of photoinduced paramagnetic centers from preexisting precursors in high-purity silicas. *Phys. Rev. B* **1990**, *41*, 7828–7834. [CrossRef]
48. Tuğay, E.; Turan, R. Investigation of Photoluminescence Mechanisms from SiO_2/Si:SiO_2/SiO_2 Structures in Weak Quantum Confined Regime by Deconvolution of Photoluminescence Spectra. *J. Nanosci. Nanotechnol.* **2016**, *16*, 4052–4064. [CrossRef] [PubMed]
49. Fauchet, P.M. Photoluminescence and electroluminescence from porous silicon. *J. Lumin.* **1996**, *70*, 294–309. [CrossRef]
50. Dohnalová, K.; Kůsová, K.; Pelant, I. Time-resolved photoluminescence spectroscopy of the initial oxidation stage of small silicon nanocrystals. *Appl. Phys. Lett.* **2009**, *94*. [CrossRef]